Berger *et al. Swiss J Geosci* (2020) 113:4
https://doi.org/10.1186/s00015-020-00356-4

SGG SGS sc | nat
Swiss Journal of Geosciences

ORIGINAL PAPER Open Access

The relation between peak metamorphic temperatures and subsequent cooling during continent–continent collision (western Central Alps, Switzerland)

Alfons Berger[1*], Martin Engi[1], Silja Erne-Schmid[1], Christoph Glotzbach[2], Cornelia Spiegel[3], Rick de Goede[1] and Marco Herwegh[1]

Abstract

The maximum temperature (T_{max}) and subsequent exhumation reflect the relations between advective and conductive heat transport, which in turn depend on the tectonic evolution. To unravel these relations in an orogen, precise T_{max} data need to be combined with relative time information for the displacements of adjacent units. We present new T_{max} data based on Raman spectroscopy of carbonaceous material (RSCM) and zircon fission track (FT) data, which are combined with previous data and then discussed jointly. We follow this approach in the Central Alps at the western edge of the Lepontine dome. Our analysis indicates two main tectono-metamorphic domains in this area: domain A comprises the Lower Helvetic units involving the Aar Massif; domain B is situated south of the Helvetic main thrust, in the footwall of the Simplon line. In domain A, thrusted Helvetic units were overprinted mainly by reverse faulting in the Aar Massif. The thermal evolution is related to the inversion of the former Doldenhorn basin. Tectonic transport during inversion brought into contact units with substantially different T_{max}. Temperature gradients were then reduced by conductive heat transfer, but thermal overprinting during cooling involved subsequent vertical movements as well. Zircon FT data yield apparent ages between 12 and 18 Ma in the external part, but 8–9 Ma in the internal part of the Aar Massif. The youngest ages are taken as the cooling at a given temperature, whereas the other data are discussed as being only partially resetted along a temperature path in the partial annealing zone of the zircon FT. When combined with age data for T_{max} and apatite FT data from the literature, the youngest group exhibits exhumation rates between 0.5 and 1.2 km/Ma in the time range between 20 Ma and today. In all of domain B, T_{max} was significantly higher than in domain A. In domain B the estimated rates of exhumation are 0.8–1.0 km/Ma for the post-20 Ma time interval. Despite of different temperature evolution, the exhumation rates are similar in both domains. The study shows the necessity to combine detailed tectonic data to interpret the T–t evolution of such an area.

Keywords: Aar Massif, Simplon, Zircon FT, RSCM, Metamorphic field gradient, Exhumation

1 Introduction

The metamorphic field gradient in an orogenic belt reflects its time-integrated thermal history, which is tightly connected to the tectonic evolution. To understand such interrelations, metamorphic data are required for each kinematic unit. In order to interpret the metamorphic field gradient dynamically, precise P–T

Editorial handling: E. Gnos.

*Correspondence: alfons.berger@geo.unibe.ch
[1] Institute of Geological Sciences, University of Bern, Baltzerstrasse 1 + 3, 3012 Bern, Switzerland
Full list of author information is available at the end of the article

constraints should be combined with temporal information, notably age data correlating to well-defined stages of the tectonic evolution. Petrochronological data (Engi et al. 2017) pertaining to the thermal peak (T_{max}) are needed, as well as data for the temperature–time evolution during cooling and exhumation. For the former, thermally robust mineral chronometers are preferable, whereas various thermo-chronometers (e.g., Wagner and van de Haute 1992; Braun et al. 2006; Malusa and Fitzgerald 2019) have often been used for cooling and exhumation stages. At any stage of an orogenic evolution, tectonic movements between adjacent units in a given time interval can severely change the thermal structure (e.g., Shi and Wang 1987; Schmalholz and Duretz 2015; Jaquet et al. 2017). During post-tectonic cooling, isotherms disturbed by tectonics will relax due to conductive heat transport. Understanding such interactions requires detailed knowledge of the geometric relationships at different times.

Here, we combine tectonic, thermometric, and geochronological data from very low-grade to amphibolite facies conditions to gain insight into the thermal structure and its evolution, especially during cooling of upper crustal levels. Such evolutions have more commonly been investigated in medium- to high-grade metamorphic terrains (e.g., Kohn 2014), but relations in very low- and low-grade areas have hardly been tested, chiefly because suitable metamorphic and petrochronological data are rarely available. We study the western end of the Lepontine dome in the Central Alps, which represents one of the well-investigated examples of a Barrovian metamorphic terrain. Several studies are available that provide details on the metamorphic field gradient (e.g., Niggli and Niggli 1965; Frey et al. 1980, 1999; Todd and Engi 1997; Engi 2011; Berger et al. 2011; Bousquet et al. 2008; Bousquet 2012; Nibourel et al. 2018). Overall, the field gradient shows spatially continuous zoning, but locally some mineral isograds (and isotherms) are offset along shear zones (e.g., Todd and Engi 1997). Such metamorphic discontinuities are most prominent near the western border of the Lepontine dome, which is the focus of this contribution. From north to south, the area studied comprises sedimentary units (Helvetic nappes) and two main basement complexes, i.e. the Aar Massif and the nappes in the Simplon area. Wedged within the latter are Valaisan metasediments, the only unit that experienced Eocene HP-LT metamorphism prior to the Oligocene–Miocene Barrovian overprint (Bousquet et al. 2008). Valaisan units in similar position at the NE-margin of the Lepontine dome show that this thermal overprint did not completely erase the Eocene imprint (Wiederkehr et al. 2009, 2011), but at the NW-margin this relation is not established (Fig. 1). In the area we studied, the overall metamorphic field gradient shows an increase from very low-grade to amphibolite facies conditions. The tectonic evolution in the area is known in some detail (e.g., Milnes 1973, 1974; Steck 1984; Herwegh and Pfiffner 2005; Krayenbuhl and Steck 2009), but the relation to the temperature–time evolution remains less clear.

Our study adds results from Raman spectroscopy of carbonaceous material and zircon fission track data to the available metamorphic and geochronological data. The combined data set is then used to quantify the field gradient reflecting the thermal maximum and the conditions of subsequent cooling. The thermal evolution in the different tectonic units involved is discussed in relation to the known tectonic phases of the orogenic evolution. We show that deformation related to the exhumation of the Lepontine dome and the uplift in frontal parts of the Central Alps created the regional metamorphic imprint now visible.

2 Tectonic and metamorphic framework

The Barrovian metamorphic dome in the Central Alps displays a continuous field gradient from very low-grade to partial melting conditions (Frey et al. 1980, 1999; Todd and Engi 1997; Bousquet et al. 2008; Bousquet 2012). The transition from greenschist to amphibolite facies conditions occurs in the Northern Steep Belt (Milnes 1974) that separates the Lepontine nappe stack from the Aar Massif adjacent to the north (Fig. 1). The Aar Massif itself has been further subdivided into its internal and external parts, and the Gastern sub-massif (e.g., Steck et al. 2001; Krayenbuhl and Steck 2009; Berger et al. 2017). During Alpine orogeny, major sediment volumes were sheared off from the crystalline basement, producing the Helvetic nappes. The sedimentary sequences are described in several contributions (Herwegh and Pfiffner 2005 and references therein). The tectonic evolution has been subdivided into two main stages (Burkhard 1988; Herwegh and Pfiffner 2005; Pfiffner 2015; Fig. 2): (1) thrusting of the main Helvetic nappes (Prabé phase); (2) inversion of an underlying basin to produce the Doldenhorn Nappe (Kiental phase; Herwegh and Pfiffner 2005). Deformation included thrusting of the Doldenhorn Nappe above the Gastern sub-massif and basement units of the external Aar Massif. Typical fold and thrust geometries developed that include basement units in internal parts of this thrust sheet. This fold and thrust belt was then overprinted by the uplift of the Aar Massif (Grindelwald phase; Burkhard 1988). Doming and uplift of the basement is connected to the internal deformation of the Aar Massif, first by reverse faulting (Handegg phase; Wehrens et al. 2017) then by NW-directed thrusting above a basal thrust system (Pfaffenchopf phase; Berger et al. 2017; Herwegh et al. 2020). Coeval with Pfaffenchopf thrusting, dextral strike-slip faulting partly affected the

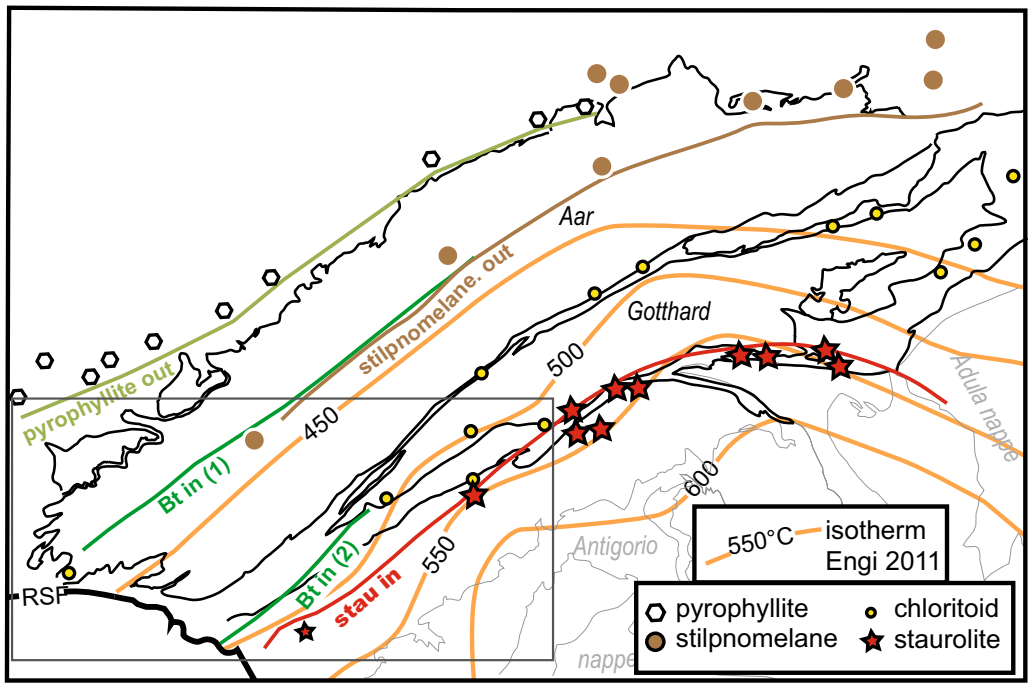

Fig. 1 Metamorphic map of the northern Lepontine dome using mineral occurrences of Niggli and Niggli (1965) and Bousquet et al. (2008). In addition, the isotherms from Engi (2011) are shown in °C. Note the end of all these data along the RSF (=Rhône Simplon fault). The area of Fig. 3 is indicated. The thick lines outline the Aar Massif and the Tavetsch and Gotthard nappes. The thin lines are the tectonic boundaries in the Lepontine

southern border of the Aar Massif (Oberaar phase, Wehrens et al. 2017). The Handegg-, Pfaffenchopf- and Oberaar phases thus represent kinematic sub-events of the Grindelwald phase (Fig. 2).

East of Brig, several units of different paleogeographic provenience are involved: continental basement and sediments from the European margin and the Briançonnais, as well as Valaisan units. These units, separated by major orogenic thrusts (i.e. Pennine front, Helvetic main thrust), underwent basement thrusting and post-nappe folding that involved both metasedimentary and basement units (e.g., Milnes 1974; Steck 1984; Sartori et al. 2017). Thrusting in this area occurred during an early stage, with coeval or slightly later isoclinal folding (D1 and D2 of Sartori et al. 2017). These deformations are responsible for nappe stacking in the Simplon area. This includes also Valaisan units, which represent the previously subducted accretionary prism (with HP-LT imprint). Further south, the Grand St. Bernard nappe-complex and equivalent gneiss sheets were interleaved with their sedimentary covers. This nappe stack subsequently became part of the lid of the future Helvetic domain (Fig. 2). The Gotthard Nappe reflects the lowest nappe of the European margin, which is thrusted on top of the Aar Massif. After the nappe geometry was established (Fig. 2), the thickened crust was then folded. This major post-nappe folding (Berisal folds) is related to the uplift of the Aar Massif (Berger et al. 2017; Ricchi et al. 2019; Herwegh et al. 2017). During and after development of these folds, the Rhône Simplon fault (=RSF) became active (e.g., Steck 1984; Mancktelow 1990, 1992; Campani et al. 2010, 2014). The RSF has a pure low angle normal fault proportion, reported at the surface as Simplon line. It continuously changes into a lateral ramp known as RSF. In the following, the Simplon fault sensu strictu and the lateral ramp will be here named as RSF (Figs. 1 and 3). At the western rim of the Aar Massif, owing to dextral slip movements, the RSF splits up into several minor branches (e.g., Campani et al. 2010; Berger et al. 2013). Movements along the RSF essentially occurred from 12 to 5 Ma, but strike-slip motion remained active up to recent times (e.g., Champagnac et al. 2003; Diehl et al. 2018).

3 Methods

3.1 Zircon fission track dating

Some zircon separates were available for dating from the samples of Reinecker et al. (2008). An additional sample set was separated at the University of Bern. This involved crushing by the SelFrag system (Giese et al. 2010). After zircon separation, minerals were mounted in PFA-Teflon and afterwards grinded and polished to expose internal

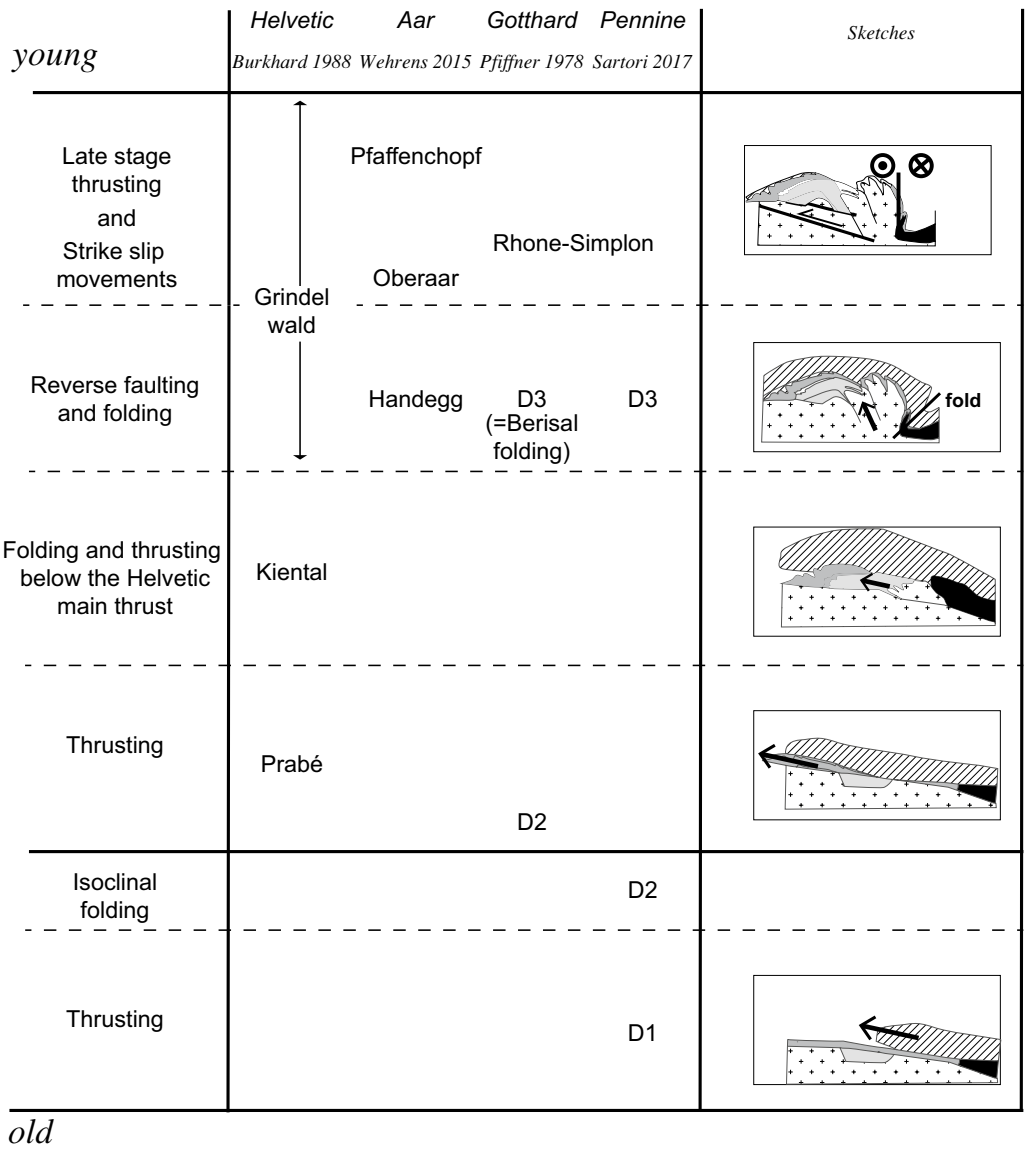

Fig. 2 Summary of the major tectonic events in the study area. Left column: the major events summarized in a given deformation phase; central column: selected literature names for the shown phases; right column: schematic sketch of the deformation; light gray: Doldenhorn Nappe, intermediate gray Upper Helvetic nappes, black: Gotthard Nappe, diagonal hatches: Penninic units. The deformation phases are sorted in relation to their structural overprint relationships, but the geodynamic processes are continuous

surfaces. After attachment of an external mica detector, thermal neutron irradiation was carried out at the FRM-II reactor (Germany). Fission track analysis was made with an optical microscope (Zeiss Axioscope 2) under 1000× magnification using a dry objective. Ages were calculated using a zeta calibration factor (zeta = 101.8 ± 0.6 a/cm^2, S. Erne-Schmid) determined on dosimeter glass IRMM-541 and Fish Canyon Tuff age standards. Calculation, visualization and statistics were performed using Trackkey 4.2 g (Dunkl 2002). All zircon fission track ages are displayed as central ages from 20 individual grains, errors shown are $\pm 1\sigma$.

The critical question, how this central zircon FT age can be used to constrain the thermal history of samples, depends on the temperature limits adopted for the partial annealing zone (= PAZ), notably its upper limit (= total stability zone) and lower limit (= total annealing zone). The absolute temperatures of both limits of the PAZ remain controversial. Here we considered limiting values of either 220° and 270 °C (Brandon et al. 1998),

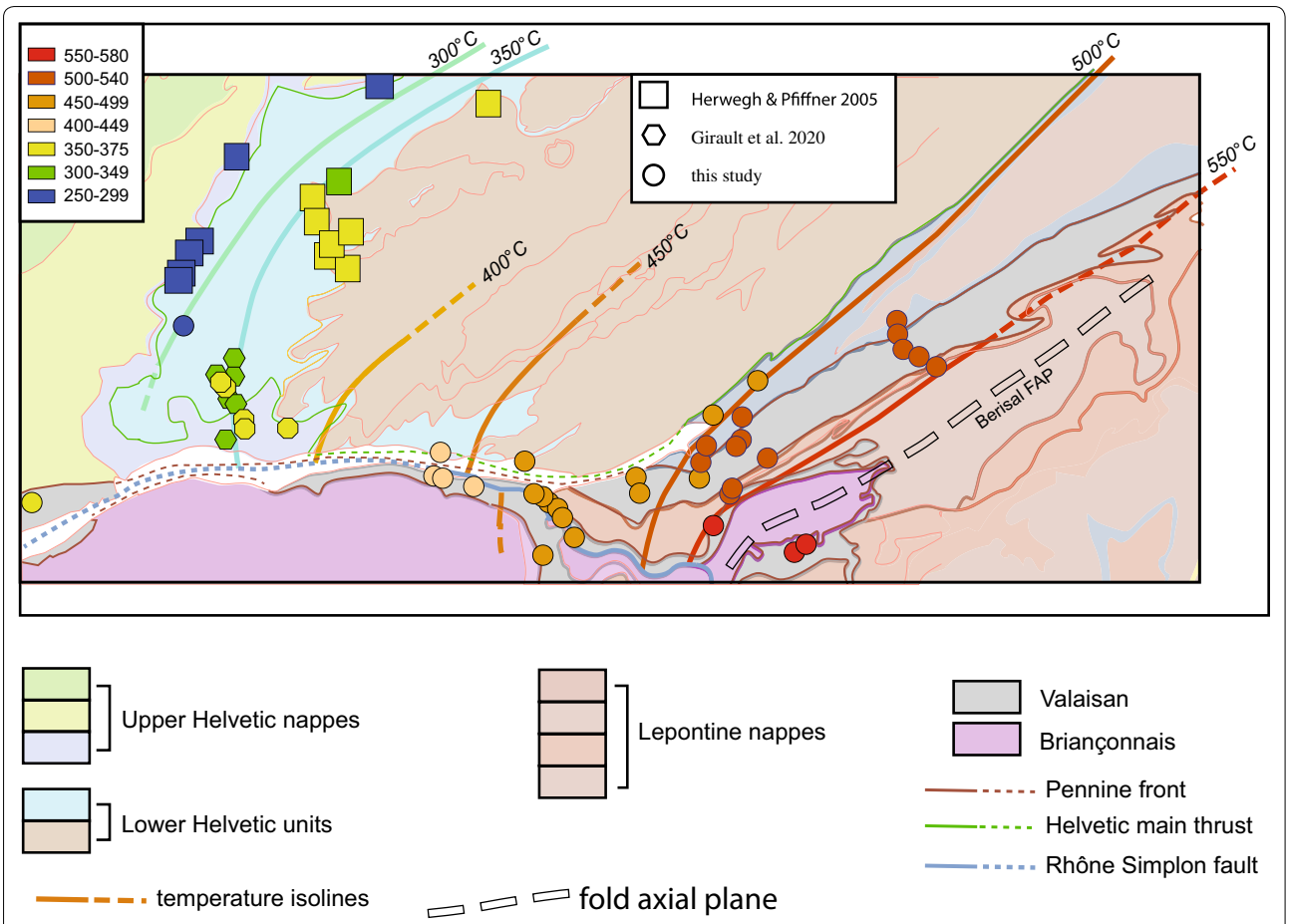

Fig. 3 Sketch map of the temperature distribution in the working area. Data points of Table 1 are shown. Isotherms are inferred. The 400 °C isotherm is based on the occurrence of Alpine biotite. See also isotherms and mineral occurrences in Fig. 1

or alternatively 230° and 330 °C (Rahn et al. 2004). The behaviour of FT inside the PAZ depends on several factors, including the time interval spent inside the PAZ (Wagner and van de Haute 1992, see also chapter 5.2) and the accumulated radiation damage (e.g., Marsellos and Garver 2010). For instance, a shorter time spent inside the PAZ (faster cooling) results in reduced annealing and higher PAZ temperatures and FT ages.

FT counting in zircons might be biased towards grains with 'countable' track densities (e.g., Rahn et al. 2019). Old and/or grains with high U content might have track densities too high to be counted accurately. Most of our samples are young and only those samples with considerable older ages (LBS-10 and LBS-11) do show low average U contents of counted grains and a general trend with lower U content associated with older ages and vice versa. This has been observed previously and interpreted to reflect radiation damage controlled differences in FT annealing (e.g., Marsellos and Garver 2010), with a negative relation between FT age and U content (or accumulated radiation damage).

3.2 Raman spectroscopy of carbonaceous material (RSCM)

Progressive heating induces ordering of carbonaceous material, changing the Raman signal. The partial ordering state of the crystalline structure can be quantified using characteristic Raman bands at certain wavenumbers (Wang et al. 1989). Beyssac et al. (2002a, b) showed that the peak intensity ratio and the peak area ratio, both calculated from bands in the first order region, are useful to quantify such changes. The peak area ratios are calibrated against temperature (Beyssac et al. 2002a, b). We performed micro-Raman spectroscopy at the Raman Laboratory of the Institute of Geological Sciences in Bern. The measurements were made using a Jobin–Yvon LabRAM HR800 instrument. A Nd-YAG continuous wave laser (20 mW beam spot of approximately 1 µm diameter, wavelength: 532.12 nm) was combined with an Olympus BX41 microscope at

100× magnification in confocal mode. The spectra were taken in the range between wavenumbers 1070 to 1750 cm^{-1}. Measurement times were 60 s. Peak fitting was done with the software "PEAKfit v4.06". The fitting itself used the Voigt area, the algorithm combined Gaussian and Lorentzian profiles. In each sample, at least ten and as many as 40 separate spots were analyzed (see Additional file 1: Appendix S1). Data sets for each sample show some scatter and occasional outliers, which probably reflect structural heterogeneity in the carbonaceous material. After removal of outliers (> 3σ), 1σ precision of the mean typically is 5–15 °C; the absolute accuracy of RSCM data is estimated at ± 50 °C. We use these measurements and calculate the weighted mean and the standard deviation as the error (see Additional file 1: Appendix S1 for more information).

4 Results

4.1 Temperature data

Sediments in the Lötschberg section have been repeatedly investigated to obtain temperature data (Williams et al. 2008; Herwegh and Pfiffner 2005; Burkhard 1988; Frey et al. 1980). Several methods were applied (Table 1): (1) $\delta^{14}C$ values, (2) calcite–dolomite (Cc–dol) thermometry, and (3) Raman spectra of carbonaceous matter. Results from the northern Aar Massif and the Doldenhorn Nappe show a steep decrease in temperature from south to north, as well as from NE to SW (Nibourel 2019). The isotherms appear to crosscut tectonic boundaries (Fig. 3; Herwegh and Pfiffner 2005; Burkhard 1988). Maximum temperatures in the Lötschberg base tunnel and the Jungfraukeil lie between 350° and 370 °C (Table 1, Figs. 3 and 4). Results from Cc–dol thermometry (Herwegh and Pfiffner 2005) and the δC^{14} (Williams et al. 2008) are consistent within the analytical uncertainties, which are in the 15–20 °C range (Table 1). In the overlying Helvetic nappes, temperatures only attained ~ 210°–250 °C (Figs. 3 and 4; Herwegh and Pfiffner 2005).

Temperature data south of the Aar Massif are available from the Gotthard- and Valaisan-metasediments (Table 1; Hafner 2016). Temperatures are ~ 470–500 °C at the contact to the Aar Massif, they increase to 550 °C in the Monte-Leone Nappe and adjacent units, and they reach 575 °C south of the Berisal fold (Fig. 3; Table 1). Toward the west, maximum temperatures were lower, reaching ~ 400–450 °C in the area of Visp (Fig. 3). In contrast to other thermochronometers the temperature data based on the RSCM method represent T_{max}. In the Simplon area these data are consistent with metamorphic multi-equilibrium thermometry (e.g., Todd and Engi 1997).

4.2 Zircon fission track data

Available zircon FT data are reported in Tables 2 and 3 (Figs. 3 and 4). Our new data extend earlier literature data (Table 2; Michalski and Soom 1990) and are consistent with these. In the Lötschberg section (Fig. 4), from north to south, a general trend is observed from older to younger zircon FT ages. We subdivide these data into three groups (see Fig. 4, Table 2): (A1) apparent mixed ages (74–110 Ma); (A2) only partially resetted ages (12–18 Ma); and (A3) cooling ages (8–9 Ma). Data in group A1 show a clear relationship between age and age scatter, which indicates slow cooling and prolonged stay in the partial annealing zone.

Data for group A2 samples show some spread in ages, with an average of 14.5 Ma (Table 2; Fig. 4). Group A3 is limited to the southern rim of the Aar Massif, recording ages of ~ 8 Ma (Table 2; Fig. 4). This age group has been related to late stage movements along the RSF (Campani et al. 2010) and/or the movements of the Rote Chue Gampel fault (Fig. 4; Sartori et al. 2017; Krayenbuhl and Steck 2009; Dolivo 1982). Our new thermochronological samples are from outcrops slightly north of the Rote Chue Gampel fault, and they appear to be related to strain distributed along this major fault (Sartori et al. 2017). In the footwall of the RSF, zircon FT ages are in the range of 10–14 Ma (Table 2, Campani et al. 2010; Soom 1990).

4.3 Timing of T_{max}

The timing of T_{max} in the Lötschberg section is not well constrained because few chronometers pertain to such low temperatures, and data tend to be difficult to interpret. K/Ar and Ar/Ar data for metasediments at the base of the Doldenhorn Nappe yield mixed ages, indicating detrital input from a Variscan hinterland mixed with sheet silicates that developed during Alpine metamorphism (Kirschner et al. 2003; Frank and Stettler 1979; Fig. 5). These data show a clear relationship between the fraction of 2M polytype of mica/illite and the ages obtained (Fig. 5). This correlation gives a first order indication about when new sheet silicates had formed in these samples. Extrapolation of the data to 100% illite-2M indicates resetting between 14 and 21 Ma. The older age group is consistent with the youngest age in Kirschner et al. (2003). The base of the Doldenhorn Nappe reached T_{max} before and during the Doldenhorn thrusting event (Kiental phase). The age of 14–21 Ma is consistent with the timing of T_{max} further east in the Grimsel area (Bt Ar-age; Rolland et al. 2009).

Valaisan units from the NE-margin of the Lepontine belt show a subduction-related HP-LT imprint of Eocene age (41.2 ± 1.2 Ma; Ar–Ar in situ white mica age;

Table 1 Summary of temperature estimates. Sources and analysts: HP05: Herwegh and Pfiffner (2005), W08: Williams et al. (2008), W13: Wicki (2014), E14: Erne (2014), G08: deGoede, H16: Hafner (2016), N13: Negro et al. (2013)

Sample	Rock type	Easting	Northing	method	Temp (°C)	Error (°C)	No. of spectra, comment	Sources/analyst
Valais/Simplon								
UG13_1a	Lower Jurassic; shale	2,668,125	1,152,708	RSCM	514	n.g.	n.g.	E14
Si1333	Lower Jurassic; shale	2,627,900	1,129,210	RSCM	438	28	*19*	H16
SE13-1	Lower Jurassic; shale	2,632,750	1,128,490	RSCM	475	22	*16*	E14
Si08A06	Slate	2,643,000	1,128,400	RSCM	530	10	*15*	G08
Si09F07	Calc-schist	2,654,950	1,136,900	RSCM	537	17	*18*	G08
Si1321	Slate	2,643,650	1,129,320	RSCM	511	16	*16*	H16
Si1325	Slate	2,645,820	1,131,020	RSCM	518	11	*18*	H16
Si1327	Calc-schist	2,644,010	1,131,360	RSCM	497	48	*24*	H16
Si1329	Calcareous micaschist	2,646,650	1,133,260	RSCM	497	27	*21*	H16
Si1438	Calcareous micaschist	2,655,030	1,136,090	RSCM	506	12	*16*	H16
Si08A01	Calcareous micaschist	2,642,800	1,128,000	RSCM	480	12	*11*	G08
Si08E02	Mica-schist	2,649,450	1,123,350	RSCM	543	46	*16*	G08
Si08E04	Mica-schist	2,648,800	1,122,900	RSCM	531	35	*15*	G08
Si09C16	Marble	2,643,700	1,124,550	RSCM	539	24	*18*	G08
Si09F06	Calcareous micaschist	2,655,050	1,136,150	RSCM	535	26	*15*	G08
Si09G01	Calc-schist	2,639,300	1,127,700	RSCM	475	27	*20*	G08
Si09G03	Marble	2,634,300	1,125,250	RSCM	460	10	*13*	G08
Si1315	Calcareous micaschist	2,630,000	1,126,370	RSCM	405	12	*16*	H16
Si1316	Marble	2,630,000	1,126,370	RSCM	426	9	*17*	H16
Si1317	Marble	2,630,000	1,126,370	RSCM	413	15	*15*	H16
Si1318	Calcareous micaschist	2,633,970	1,122,440	RSCM	463	31	*24*	H16
Si1319	Calcareous micaschist	2,633,920	1,122,650	RSCM	415	15	*16*	H16
Si1320	Calcareous micaschist	2,633,920	1,122,650	RSCM	460	34	*24*	H16
Si1323	calcareous micaschist	2,645,640	1,129,530	RSCM	509	15	*18*	H16
Si1324	Calc-schist	2,645,640	1,129,530	RSCM	532	26	*21*	H16
Si1436	Calcareous micaschist	2,639,630	1,126,490	RSCM	456	14	*15*	H16
Si1440	Calcareous micaschist	2,627,730	1,127,890	RSCM	401	14	*16*	H16
Si1441	Marble	2,635,970	1,124,360	RSCM	454	11	*14*	H16
VS0704	Zone Sion Courm.	2,627,274	1,127,885	RSCM	447	20	*10*	N13
VS0705	Zone Sion Courm.	2,602,170	1,125,880	RSCM	361	9	*12*	N13
VS0706	Zone Sion Courm.	2,603,680	1,126,060	RSCM	382	6	*10*	N13
VS0707	Zone Sion Courm.	2,604,580	1,125,600	RSCM	385	9	*12*	N13
VS0801	Zone Sion Courm.	2,631,799	1,126,779	RSCM	465	28	*15*	N13
VS0802	Zone Sion Courm.	2,629,896	1,126,727	RSCM	453	13	*13*	N13
VS0804	Zone Sion Courm.	2,645,239	1,128,191	RSCM	543	29	*14*	N13
VS0806	Zone Sion Courm.	2,633,885	1,122,590	RSCM	461	12	*12*	N13
Si08C14	Calc-schist	2,645,050	1,126,650	RSCM	523	14	*12*	G08
Si09F02	Calc-schist	2,656,200	1,134,700	RSCM	533	28	*15*	G08
Si09F05	Calc-schist	2,655,000	1,135,750	RSCM	542	22	*19*	G08
Si09G02	Calc-schist	2,634,150	1,126,500	RSCM	466	21	*18*	G08
Si09R01	calc-schist	2,647,350	1,128,400	RSCM	495	19	*15*	G08
Si1311	Calcareous micaschist	2,632,770	1,127,250	RSCM	421	7	*n.g.*	H16
Si1312	Calc-schist	2,632,860	1,127,230	RSCM	497	29	*26*	H16
Si1314	Mica-schist	2,633,460	1,126,790	RSCM	490	29	*24*	H16
Si08C13	Quartzite	2,645,150	1,126,150	RSCM	521	14	*14*	G08
Si09F01	Calc-schist	2,656,700	1,134,500	RSCM	534	40	*20*	G08
Si1313	Calcareous micaschist	2,633,090	1,126,880	RSCM	489	14	*26*	H16

Table 1 (continued)

Sample	Rock type	Easting	Northing	method	Temp (°C)	Error (°C)	No. of spectra, comment	Sources/analyst
Si1439	Mica-schist	2,659,520	1,135,550	RSCM	584	29	*16*	H16
Jungfraukeil								
JUNG986	Quinten-Fm, limestone	2,623,550	1,138,800	Cc–Dol	385	16		HP05
FT1–FT4	Carbonif.; coal-shale	2,623,988	1,137,016	∂C Eqn. 2	327	n.g.	291 ∂C Eqn. 1	W08
BT1–BT2	Carboniferous coal	2,624,105	1,137,070	∂C Eqn. 2	354	n.g.	313 ∂C Eqn. 1	W08
Kandertal								
K-14WB277	Quinten-Fm, limestone	2,618,800	1,145,000	Cc–Dol	348	14		HP05
K-14WB1.50	Quinten-Fm, limestone	2,618,800	1,145,000	Cc–Dol	350	18		HP05
Do-28	Vein in Quinten Fm.	2,623,300	1,141,850	Cc–Dol	351	16		HP05
Do-28	Vein in Quinten Fm.	2,623,300	1,141,850	RSCM	343	15		W13
BT3–BT5	Carboniferous coal	2,619,624	1,143,808	∂C Eqn. 2	347	n.g.	307 ∂C Eqn. 1	W08
BT6	Carboniferous coal	2,618,720	1,145,060	∂C Eqn. 2	357	n.g.	316 ∂C Eqn. 1	W08
Do-8	Quinten-Fm, limestone	2,622,700	1,144,525	Cc–Dol	350	n.g.		HP05

Comments: Italic numbers are the numbers of spectra analysed. Easting, Northing Swiss coordinates

RSCM Raman spectroscopy of carbonaceous material, *Cc–dol* calcite–dolomite thermometry, *∂C* carbon isotopic thermometry. *n.g.* not given. For methods see Additional file 1: Appendix S1

Wiederkehr et al. 2009). Inside the Barrovian (medium pressure) amphibolite facies belt, the Valaisan units were overprinted at ~25 Ma (Wiederkehr et al. 2009). Early Alpine HP-LT conditions are also known from the Valaisan units to the W and SW of the Simplon area; while not dated, these are presumed to be Eocene as well (Villa et al. 2014). This indicates different P–T paths for the Valaisan units compared to their surroundings (see Berger et al. 2011 for discussion). The potential nearly isothermal decompression and/or additional heating during Barrovian overprint allow a different T_{max} in the Valaisan units as in the sediments without an HP-LT event. For the northern Lepontine belt in general, few petrochonological data date prograde mineral growth to amphibolite facies conditions. In the Simplon area (Steinental), Vance and O'Nions (1992) found prograde garnet growth using Sm/Nd methods between 32 and 25 Ma, but these data may not date the thermal peak. In the northern part of the Lepontine belt, T_{max} is best constrained at 18–19 Ma (Janots et al. 2009), but only in samples some 50–70 km NE of Simplon pass. Th/Pb data in samples from the Robiei area (~17 km ENE of Simplon) show allanite growth at 20 Ma at T_{max} (Boston et al. 2017). Further south (N of Domodossola) the same study found monazite growth at 22 Ma, also near T_{max}. All of these late Oligocene to early Miocene ages reflect conditions that postdate nappe stacking, but are close to T_{max}.

5 Discussion

5.1 Thermo-tectonic domains

As mentioned in the introduction, understanding how a metamorphic field gradient formed, requires insight from the distribution of T_{max} data and their age. The study area, from the Kander valley to the Simplon area, encompasses a wide range of metamorphic temperatures and tectonic evolution. These differences are not readily visible in the metamorphic field gradient documented by various studies, which seems to be continuous (Figs. 1 and 2; Bousquet 2012). In order to discuss the thermal evolution, we subdivide the area into following major tectonic domains (Fig. 6): (A) The Lower Helvetic nappes and the Aar Massif; (B) the footwall of the RSF south of the Gotthard Nappe; and (C) the hanging wall of the RSF, which will not be analysed in this contribution.

The Upper Helvetic nappes are separated from the Lower Helvetic nappes by the Helvetic main thrust (Figs. 3 and 6). The units below this thrust include the Aar Massif and the Doldenhorn Nappe, i.e. our domain A. It is characterized by an eroded lid, owing to thrusting above the Lower Helvetic nappes and the Aar Massif before domain A reached T_{max}. The exact timing for T_{max} is a matter of debate, but relative age constraints show that T_{max} in this domain occurred during or shortly after nappe stacking (e.g., Burkhard 1988; Herwegh and Pfiffner 2005). Domain B differs in this respect, as nappe stacking precedes T_{max} by several millions of years (Berger et al. 2011; Boston et al. 2017). A clear temperature hiatus is evident along the RSF (Bousquet 2012; Frey et al. 1999, Fig. 3).

In domain B, the metamorphic and structural imprint shows marked spatial gradients, indicating late-Alpine tectonic effects (Fig. 8, Campani et al. 2014). These are primarily due to the development of the Berisal fold with its axial plunge, the 3D projections of which are visible

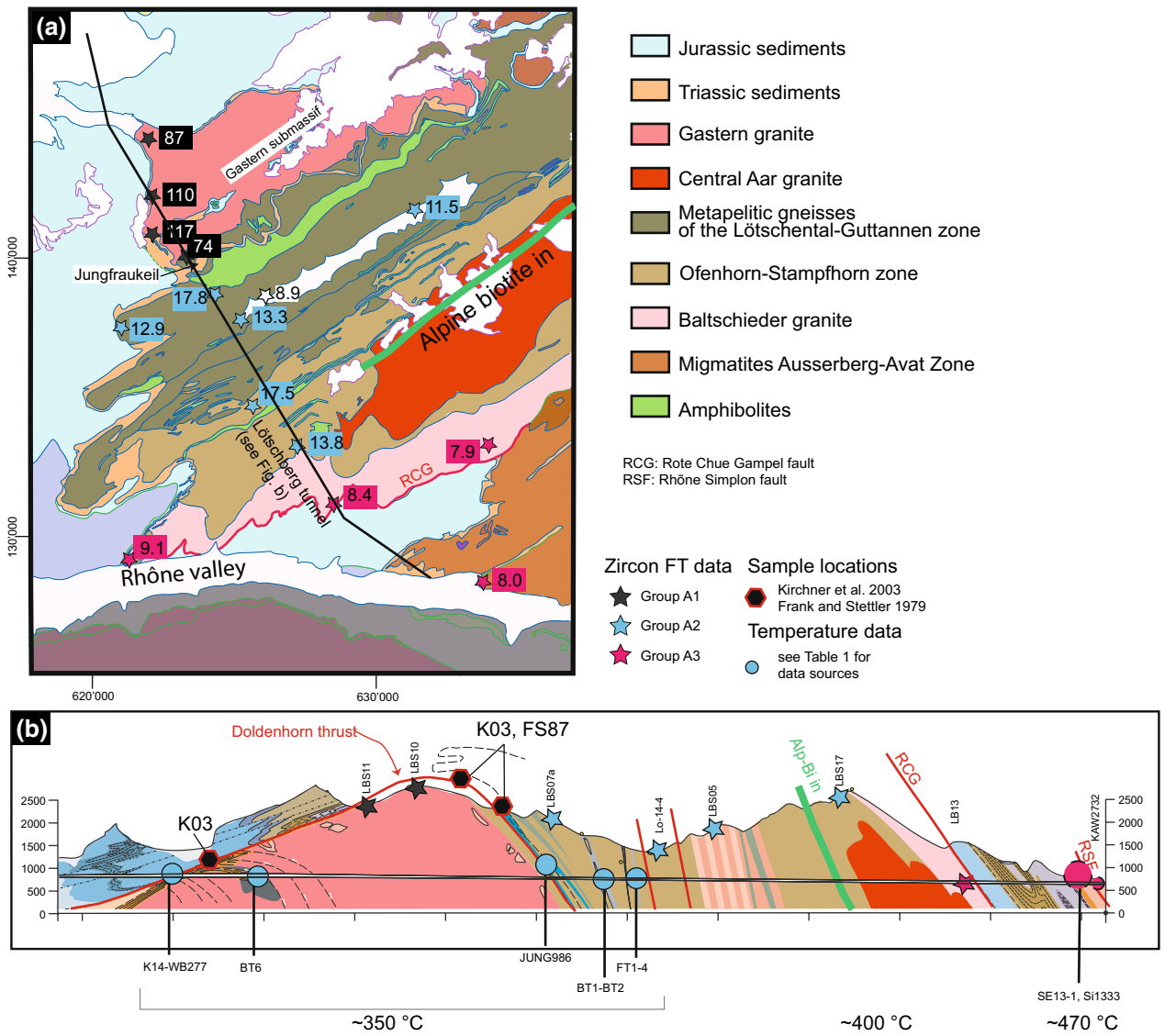

Fig. 4 Geological map (adapted from Berger et al. 2017) of domain A with metamorphic and thermochronology data. **a** Western Aar Massif with available zircon FT data, **b** cross section along the Lötschberg base tunnel (modified after Ziegler and Isler 2013) with zircon FT and temperature data. *RCG* Rote Chue Gampel fault

in the structural profiles (e.g., Schmidt and Preiswerk 1905; Milnes 1973; Steck 1984, 2008) and in 3D structural models (Campani et al. 2014). A reorientation of the metamorphic field gradient has been proposed (Chatterjee 1961; Streckeisen et al. 1974) based on the combination of mineral assemblages observed in the Simplon tunnel with those documented from surface outcrops (up to 1 km above the tunnel-level).

5.2 Interpretation of the zircon FT ages

The zircon FT ages are grouped into: (A1) apparent ages between 74 and 117 Ma in the Gastern sub-massif; (A2) ages between 12 and 18 Ma in a central section; and (A3) ages between 8 and 9 Ma in the south (Fig. 4). The geological meaning of such FT data depends on different parameters, which are under debate (e.g., Rahn et al. 2019, Tagami and Matsu´ura 2019). Additional information to the age will be, for example, gained by FT length measurements (Rahn 2001; Rahn et al. 2019). Our samples are not well suitable for statistical robust length measurements. However, the length inspection indicates shorter FT length in samples of group A2 in comparison to group A3. This implies an incomplete or partial resetting, which can be either explained by a prolonged stay

Table 2 Summary of used geochronological data

Sample	Location	Group/domain				Zir FT age	Ap FT age	References
		Name	East	North	Elevation	Ma	Ma	
LBS-10	Lötschberg	A1	2,621,770	1,141,060	2830	73.8	9.4	ts R08
LBS-11	Gletschertor	A1	2,621,120	1,142,000	2364	109.7	10.5	ts, R08
LBS-05	In Steinigen Gräbun	A2	2,625,000	1,136,280	1850	17.5	7.0	ts, R08
LBS-07	Fleischweng/Restialp	A2	2,623,240	1,138,400	2090	17.8	8.1	ts, R08
LBS-17	Mallich	A2	2,626,540	1,132,780	2700	13.8	7.5	ts, R08
Lo-14-2	Lötschental	A2	2,631,342	1,142,112	1700	11.5	–	ts
Lo-14-4	Lötschental	A2	2,624,256	1,135,893	1300	13.3	–	ts
LB-13	Baltschieder-Granodiorit	A3	2,625,700	1,130,000	641	8.4	3.4	ts, R08
KAW2617	Niedergampel	A3	2,621,150	1,129,200	660	9.1	3.8	MS90
KAW2782	Baltschieder	A3	2,632,949	1,128,330	650	8.0	1.7	MS90
KAW2780	Wiwannihorn	A3	2,632,470	1,133,050	2540	7.9	3.6	MS90
KAW2616	Staldi	A1	2,620,775	1,144,600	1440	86.9	5.1	MS90
KAW2702	Hockenhorn	A1	2,623,700	1,141,525	3020	117	6.8	MS90
KAW2664	Lötschberg	A2	2,622,150	1,139,300	1220	12.9	8.8	MS90, R01
KAW65	Tenmatte	–	2,627,850	1,140,150	1460	8.9	3.5	MS90, W77
KAW 519	Salweide	C	2,621,100	1,123,000	1500	22.3	10.8	S90
KAW 520	Moosalp	C	2,629,850	1,122,750	2020	19.8	7.2	S90
KAW 2761	Eggishorn	A2	2,650,310	1,141,880	2870	11.7	5.6	S90
KAW 2779	St. Luc	C	2,612,600	1,118,140		–	11.7	S90
KAW 404	Embd	C	2,630,200	1,117,900	1200	–	4.9	W77
MC482		B	2,637,778	1,127,174	830	9.7	–	C10
MC335		B	2,640,487	1,127,471	1181	10.9	–	C10
MC480		C	2,633,106	1,126,381	1152	14.1	–	C10
MC481		C	2,634,746	1,124,983	902	13.7	–	C10
KAW 164	Eisten-1	B	2,647,060	1,127,550	1410	–	4.2	W77
KAW 165	Eisten-2	B	2,646,540	1,127,540	1390	–	4.4	W77
KAW 409	Spitzhörnli	B	2,642,100	1,123,600	2600	–	6.7	W77

ts this study (see Table 3), MS90: Michalski und Soom, R08: Reinecker et al. (2008), S90: Soom (1990), C10: Campani et al. (2010), W77: Wagner et al. (1977), R01: Rahn (2001)

Table 3 Results of the zircon fission track analysis

Sample	U ppm	Cryst. No.	Spontaneous		Induced		$P(\chi)^2$	Dispersion	Age	Error
			ρ_s	N_s	ρ_i	N_i	%		Ma	Ma
LBS-05	653	20	52.8	259	102.2	482	71.3	0.02	17.5	±1.7
LBS-07	704	20	57.7	289	109.7	550	63.9	0.01	17.8	±1.7
LBS-10	421	18	145.1	428	66.1	195	33	0.1	73.8	±7.9
LBS-11	339	20	172.7	594	52.6	181	65.4	0.02	109.7	±11.5
LBS-17	1102	19	73.9	305	179.7	742	34.2	0.18	13.8	±1.3
Lo-14-2	988	20	49.6	278	147.2	825	2.5	0.25	11.5	±1.1
Lo-14-4	909	20	60.1	307	154.2	788	26	0.06	13.3	±1.2
LB-13	699	20	24.1	356	110.3	1627	31.6	0.09	8.4	±0.7

Ages were calculated using the zeta calibration method (Hurford and Green 1983), glass dosimeter IRMM541, and a zeta value of 101 ± 8 year/cm^2 (S. Erne-Schmid) calculated with Fish Canyon Tuff zircon standards

ρ_s: the spontaneous (induced) track density (105 tracks/cm^2); N_s: the number of counted spontaneous (induced) tracks; ρ_d: the dosimeter track density (105 tracks/cm^2); N_i: the number of tracks counted on the dosimeter; $P(\chi)^2$: the probability of obtained Chi-square value for n degree of freedom (where n is the number of crystals minus 1)

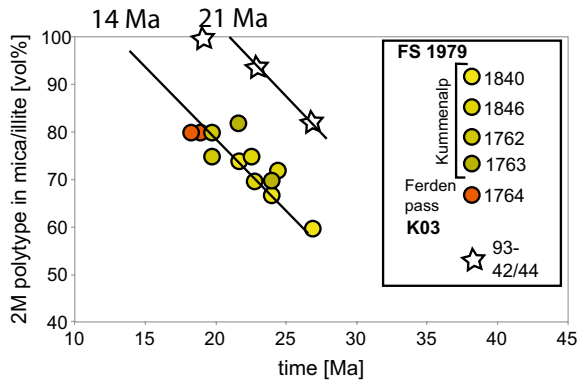

Fig. 5 K–Ar data of Frank and Stettler (1979, FS79) and Ar–Ar data of Kirschner et al. (2003, K03) in a diagram of mica composition against apparent age. The trends of the samples that belong to metasediments of the Doldenhorn Nappe indicate an upper intercept at 14 and 21 Ma with 100% illite-2M

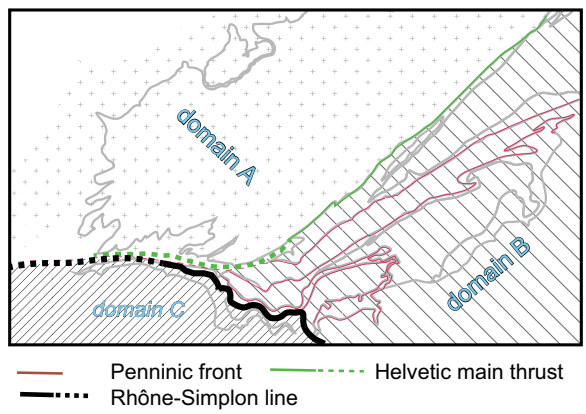

Fig. 6 The tectono-metamorphic domains of the study area. Note the repetition of the Pennine frontal thrust due to folding

in the PAZ due to slow cooling or by insufficient high temperatures during maximum burial of group A2 samples. Sample MRP205 from Rahn (2001) shows a negatively-skewed length distribution, indicating also an incomplete or partial resetting of the zircon FT inside this sample, located west of the study area inside the Rawil depression (Leuk area; Rahn 2001). Incomplete or partial resetting of FT is also indicated by a large spread in zircon FT ages in group A2. In contrast, the samples of group A3 reached temperatures high enough for complete resetting of FT and cooled faster and therefore have tentative longer track length. The group A2 ages indicate an average of 14.5 Ma, but the observations summarized above suggest that this may be not a geological significant age. Sample KAW65 (not included in group A2) is also located in the area of group A2, but shows an age of only 9 Ma (Michalski and Soom 1990). This could be related to local complete resetting and/or slightly different annealing kinetics (depending on U content, fluids, etc.). Therefore, we mention in the following group A2 as an average age of 14.5 Ma, but interpret this as an age with incompletely/partially reset FT. In contrast, the constant age of 8-9 Ma in group A3 is interpreted as a cooling age.

5.3 Domain A: Thermal and tectonic interplay in the Aar Massif

The above defined age groups in the Lötschberg section (Fig. 4) are compared with temperature data from nearby locations. The temperature data are limited to the metasediments, which are grouped into samples between the front of the Gastern sub-massif to the Lötschen valley (=group X) and samples near the southern rim of the Aar Massif (=group Y). Temperature data in group X are not from the same tectonic units as the zircon FT data of group A1. The mixed zircon FT ages from group A1 reflect lower T_{max} than group A2. Using the results of the FT data and the different T–t evolution between group A1 and A2 samples implies that T_{max} in this area must have been reached before the present day geometry was established, i.e. before the Kiental deformation (compare sample location marked by black stars with those shown by black circles in Fig. 7b). In a next stage, during Kiental thrusting, samples of group X (temperature) were brought into direct contact with group A1 samples. This is related of the tectonics of the inversion of the Doldenhorn basin, which includes decoupling between the basement and the sediments. Coevally, the Jungfraukeil developed at this deformation phase, as did the related mylonites (Herwegh and Pfiffner 2005). This phase is responsible for producing a new generation of sheet silicates, which yield ages of 20–22 Ma (Fig. 5, Kirschner et al. 2003). At this stage, the fold and thrust geometry of the Doldenhorn Nappe developed, and deformation occurred also in basement units indicating a change from thin-skinned to thick-skinned tectonics (Herwegh and Pfiffner 2005; Krayenbuhl and Steck 2009). This deformation bent the isotherms, an effect also found in thermo-mechanical models simulating the evolution of fold and thrust belts (e.g., Shi and Wang 1987; Schmalholz and Duretz 2015; Jaquet et al. 2017). The geometry and elapsed time assumed in a thermo-mechanical model of Jaquet et al. (2017) corresponds well with the situation of the Doldenhorn Nappe (Fig. 7, Jaquet et al. 2017 their Fig. 4). The above-mentioned transport between group A1 and group X samples developed during the thrusting of the Doldenhorn Nappe (Fig. 7 compare a and b). Reverse faulting movements along steep SE dipping

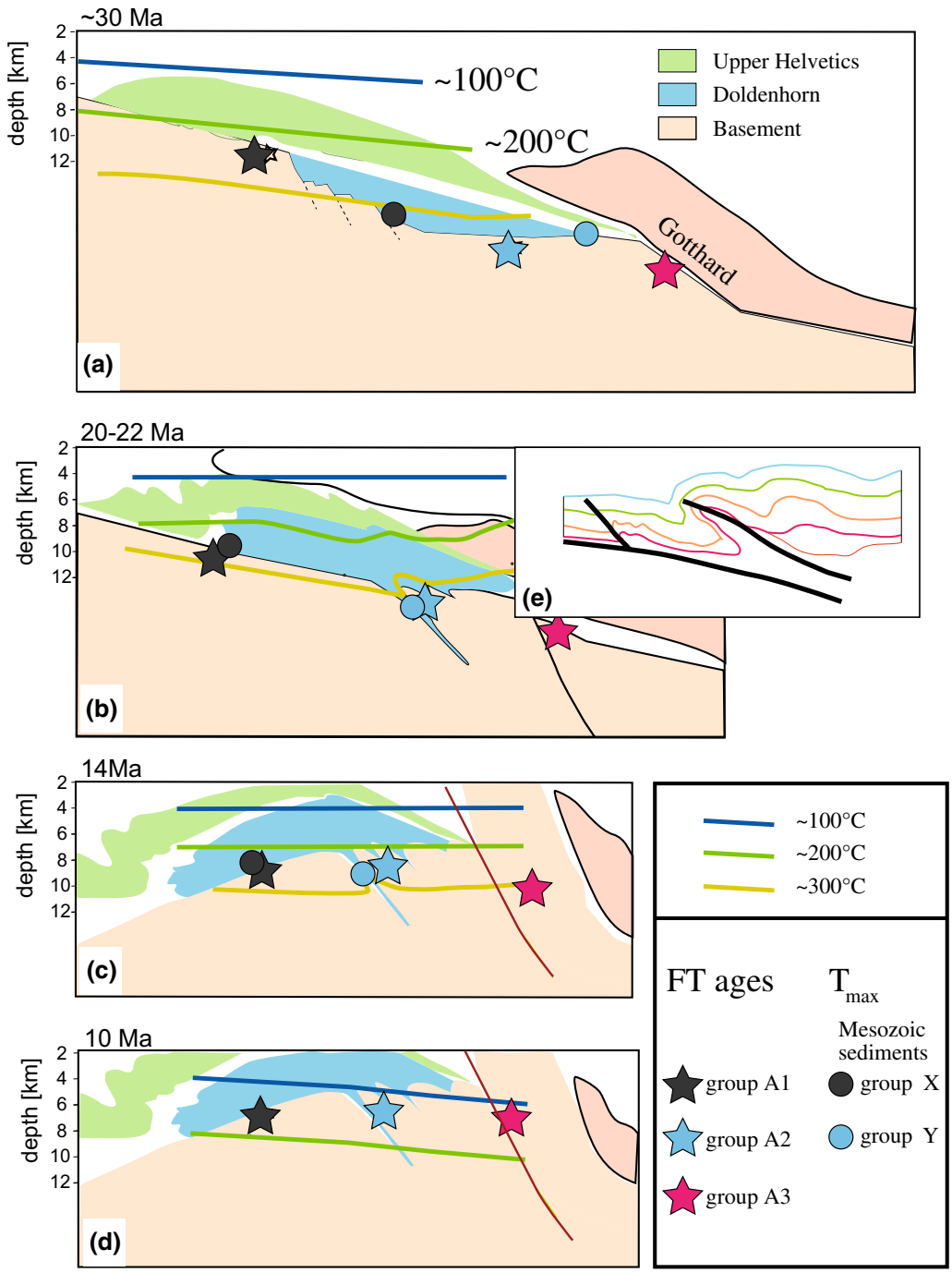

Fig. 7 Tectonic evolution of Domain "A" inspired by Herwegh and Pfiffner (2005). Stars represent zircon FT samples. Circles represent samples used for thermometry in each group, respectively, **a**–**d** show different time steps of the tectonic evolution. **a** The present day close by locations of zircon FT samples of group A1 and T_{max} samples of Group X have large distance in the situation before inversion of the Doldenhorn basin. **e** Redrawn from temperature modelling of Jaquet et al. (2017, their Fig. 4)

shear zones and foliation planes during the subsequent Handegg deformation phase allowed for partial conductive equilibration of the isotherms. This is indicated by similar T_{max} in the Kander valley and in the Jungfraukeil, despite the teconically doming between these two areas (Fig. 7c; Herwegh and Pfiffner 2005). The doming and related numerous zones of Handegg deformation allow the occurrence of the samples of group A1 and A2 at

different time intervals in the PAZ of the zircon FT (see also Sect. 5.2). The group A2 samples are more reset-ted as samples of group A1. During the combination of reverse faulting and the relaxation of the overturned isotherms by conduction, these samples passed through the zircon PAZ, but still did not allow complete resetting of the FT (see Sect. 5.2). The group A3 samples are related to temperatures of group Y and show faster differential uplift (Fig. 7d). The apatite FT ages of the same samples show also a difference between group A2 and A3, indicating differential movements between the internal and external Aar Massif (Reinecker et al. 2008).

5.4 When did the Valaisan units reach T_{max}?

Within the Simplon nappe stack (domain B), tectonic slices of Valaisan metasediments occur interleaved and post-nappe folded with other units (e.g., Bousquet et al. 2008). In corresponding units near the NE margin of the Lepontine dome, isotherms associated with the Barrovian overprint crosscut refolded nappe contacts (Fig. 1, Wiederkehr et al. 2008). In an area further east, several units—notably the Valaisan and the Adula—reflect bimodal P–T paths, with some rocks retaining their HP-imprint. Hence these units attained T_{max} earlier, in the Eocene (40–42 Ma, Wiederkehr et al. 2009, see also discussion in Villa et al. 2014) compared to the Barrovian overprint (16–19 Ma, Wiederkehr et al. 2009; Allaz et al. 2011; Boston et al. 2017). To the west of the Simplon area, RSCM data for three Valaisan samples from the north flank of the Rhône valley (Sion-Courmayeur Zone) indicate RSCM-temperatures of 361 ± 9 to 385 ± 9 °C (Table 1). In the Simplon area (between Brig and Monte Leone), sparse HP-relics occur in Valaisan rocks (e.g., chloritoid + pseudomorphs after carpholite; Bousquet et al. 2008), but no intact HP-assemblages have been reported. Contacts between Valaisan slivers and adjacent metasedimentary and gneissic units are sheared and jointly folded. This implies that the (post?-) Eocene decompression of the Valaisan slices preceded the formation of the Simplon nappe stack. In the eastern Lepontine, Wiederkehr et al. (2008, 2009, 2011) attributed decompression and nappe stacking to the same orogenic stage including different P–T paths depending on the amount of heating (Wiederkehr et al. 2008, 2011; Berger et al. 2011; Roselle et al. 2002). Therefore, it is not clear at what stage the Valaisan units in the Simplon area reached T_{max}. In an attempt to clarify the situation, RSCM data were scrutinized for each tectonic unit by Hafner (2016; using weighted kriging analysis). This study applies the weighted kriging to (a) the separate datasets from each unit, and (b) jointly for all of the units in the nappe stack (NE of the Simplon-Rhône line). The analysis showed that the resulting isotherm patterns for (a) and (b) are not significantly different. As the spatial T_{max} pattern for the samples from Valaisan units is the same (within error) as for the adjacent units, we surmise that they are likely to be of the same age and thus that T_{max} in domain B was attained during or after formation of the Simplon nappe stack.

5.5 The metamorphic field gradient

In external parts of the Lepontine belt, the metamorphic field gradient of the Barrovian metamorphism is oriented subparallel to the structural domains, such as the Aar Massif and the Gotthard Nappe (Fig. 1). This is well visible from the mapped mineral isograds and isotherms (e.g., Bousquet 2012; Todd and Engi 1997; Niggli and Niggli 1965; Fig. 1). In contrast, near the triple junction of the RSF, Helvetic thrust and the Pennine front in the Rhône valley, this simple relationship is lost (Fig. 8, Streckeisen et al. 1974; Milnes 1975; Chatterjee 1961). This perturbation may be related to: (1) tectonic transport after T_{max}; (2) a 3D sectional effect (compare Figs. 3 and 8, Campani et al. 2014); (3) variable timing of T_{max} in different units.

It has been proposed early, that the metamorphic field gradient is steep in the area south of Brig (Streckeisen et al. 1974; Chatterjee 1961; see also Fig. 8). The projection of all available data (this study) into a profile allows such an interpretation (Fig. 8). At a larger spatial scale, the thermal field gradient is steep in the front of the Aar Massif (Mair et al. 2018; Nibourel 2019; Fig. 8). In southward direction, it shows a gradual increase to lower amphibolite facies, followed by a second marked increase in the region of the Berisal fold (Fig. 8). In any case, isotherms are bent and crosscut tectonic boundaries (Fig. 8). In order to explain such a field gradient, three possibilities are envisaged as idealized end member scenarios (Fig. 9): (1) metamorphic data may reflect (static) thermal relaxation after thrusting and folding (Fig. 9e); (2) metamorphic data may reflect conditions after thrusting, but before folding (Fig. 9b), or (3) metamorphic data may reflect conditions that postdates thrusting and folding (Fig. 9c). In the area between the Aar Massif and the Berisal fold, the field gradient visible does not correspond to any such end member. Instead, a combination of thrusting and folding was involved (Figs. 7 and 9d). The inferred isotherms are a combination of thrusting, folding and conductive heat exchange at conditions near T_{max} (Fig. 9d). This metamorphic situation is later followed by exhumation and cooling (Sect. 5.6).

Considering the temporal relations, the older nappe stack south of the Aar Massif (domain B) reached T_{max} (at ~ 20 Ma), i.e. well after nappe stacking (e.g., Wiederkehr et al. 2009, Berger et al. 2011). However, T_{max} was reached, while nappe formation occurred further north

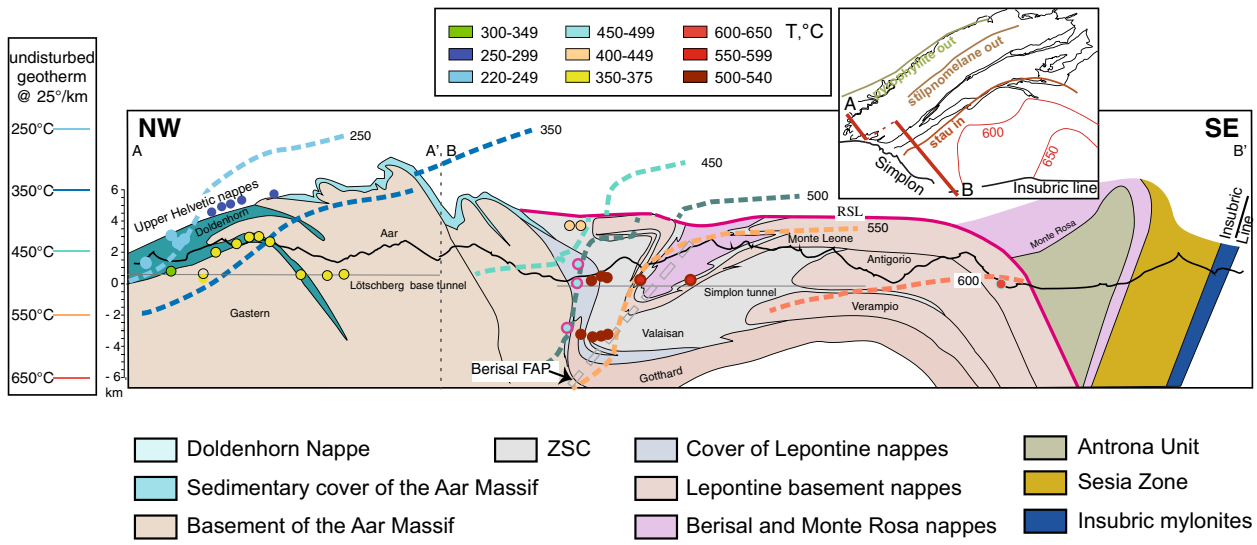

Fig. 8 Schematic profile from Domodossola to the Kander valley depicting the temperature distribution. RSCM data were projected into the plane of the cross section. Color coding for temperature is shown above the profile. Small inset map (top right) shows metamorphic reaction isograds and maximum isotherms within the Aar/Gotthard massifs and northern Lepontine dome and the traces of the two cross section parts. For reference only, a geothermal gradient of 25 °C/km is shown to the left of the section. Cross section A–A′ inspired by Ziegler and Isler (2013) and Herwegh and Pfiffner (2005), cross section B–B′ modified after Campani et al. (2014). The data point at the 600 °C isotherm in the south is based on sample Si9410 of Todd and Engi (1997). The slight shift between the contour line and the single data point is based on the contouring. *ZSC* Zone of Sion Courmayeur (Valaisan), *FAP* fold axial plane

(Doldenhorn Nappe; domain A; Figs. 2, 4, 8). In domain B the T_{max} structure was reached after decompression and nappe stacking (at ~20 Ma, Sect. 5.1). This T_{max} structure was then modified by folding (Berisal fold) and subsequently underwent a limited overprint by conductive heat transfer (Fig. 8). The Berisal folding is connected in time and kinematics to the uplift of the Aar Massif (Handegg deformation-phase, Fig. 2, see also Campani et al. 2010, 2014).

5.6 Cooling/exhumation rates

As discussed above for the timing of T_{max}, the cooling (and related exhumation) will give insights into the post-T_{max} tectonics. The apparent cooling rates are derived from T_{max} data and the assumed temperature value of the closure for the apatite and zircon FT (see also Sect. 5.2). Average values are estimated locally to obtain local cooling rates, which are then transferred into exhumation rates on the basis of an assumed average geothermal gradient of 25°/km. These calculations yield exhumation rates between 0.5 and 1.2 km/Ma (Fig. 10; Table 4). We can further subdivide the area in the external and internal Aar Massif and the domain B including the area of the Monte Leone Nappe and the Berisal area (Figs. 7 and 10). This subdivision shows the general increase of cooling rate from the Aar Massif to the Monte Leone Nappe for the youngest interval (Fig. 10). The estimated exhumation rates in the Aar Massif are in agreement with available results of thermal modelling from Reinecker et al. (2008). These calculations yield exhumation rates between 0.5 and 1.2 km/Ma (Fig. 10, Table 4). We can further subdivide the area in the external and internal Aar Massif and the domain B including the area of the Monte Leone Nappe and the Berisal area (Figs. 7 and 10). The calculated exhumation rates in the Aar Massif are in agreement with available results from thermal modelling by Reinecker et al. (2008). In general, cooling initially following T_{max} was slow, which may indicate dominantly conductive heat flow without substantial exhumation. In a second phase, cooling attended uplift and exhumation of the orogenic domains in their final tectonic geometry. The time interval of rapid cooling (and exhumation) changed over time, and the highest present day exhumation and cooling rates are located in the southern Aar Massif (e.g., Herwegh et al. 2020).

6 Conclusion

This study discusses: (1) how apparent cooling rates are influenced by tectonics in low-grade metamorphic units; and (2) how major tectonic boundaries were active at different times leading to a separation into thermo-tectonic domains:

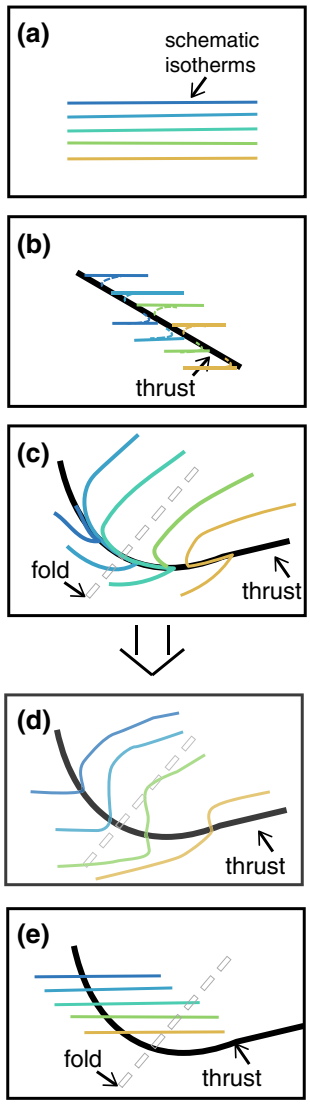

Fig. 9 Geometric relationships between tectonic boundaries and maximum metamorphic temperature in cross section view. Colored lines are schematic isotherms, black lines are tectonic boundaries: **a** initial undisturbed thermal structure, **b** thrusting outlasts metamorphism; **c** metamorphism predates thrusting and folding; **d** partial thermal reequilibration after the situation in (**c**); **e** post-tectonic metamorphism

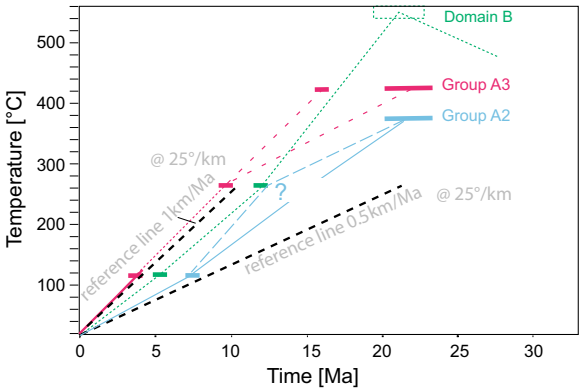

Fig. 10 Time-temperature evolution for the different domains. Time against temperature coloured bars show the age of centered closing temperatures of the used chronometers (see Table 4)

- In domain A, the sediments in the Lower Helvetic units (Aar Massif and Doldenhorn Nappe) record the inversion of a sedimentary basin with a thrust and fold geometry and subsequent thermal equilibration by conduction. These processes occurred in a time interval of 5–10 million years, whereas the developed geometry is maintained during subsequent exhumation in a block-like manner and over a longer time span.
- In domain B a deeper crustal level is exhumed, where the nappe stack developed over several million years related to deformation of D1 and D2 in the sense of Sartori et al. (2017) (Fig. 2), and T_{max} was reached after nappe stacking. The thermal structure of domain B was folded at km-scale at conditions near T_{max}, which did not result in a passively folded T_{max} structure, since the metamorphic field gradient may have been slightly modified after folding, but prior to regional cooling.
- While nappe stacking occurred in domain A, T_{max} was reached in domain B several million years after nappe stacking in this area.
- The isotherms were locally bent due to late exhumation of the Aar Massif (including Berisal folding).
- Exhumation rates estimated from FT data range between 0.7 and 1.5 km/Ma.

Data using the RSCM method have proven to be suitable to refine and extend data on T_{max} in a classic Alpine terrain that has seen a complex tectonic and metamorphic evolution. To understand the metamorphic imprint and field gradient properly, it is critical to combine thermal data with low-temperature age constraints, which are here based mostly on zircon and apatite FT data. A complete discussion of the interplay between deformation and thermal effects would require a 3D view of the evolution, taking into account the influence of strike-slip faults in particular. However, the data presented here confirm the sensitive interdependence of the tectonic and metamorphic evolution, which is well established for high-grade terrains (e.g., Nepal Himalaya, Kohn 2014), but it is here confirmed also at low to medium grade.

Table 4 Estimated exhumation rates for the different domains (see text for explanation)

	Stage 1 (T_{max}-ZFT)	Stage 2 (ZFT-AFT)	Stage 3 (AFT-surface)	Samples used
Domain A3	0.7	1.2	1.5	LB13, KAW2617, -2782
Domain B	0.9	1.0	0.8	MC482, -335, KAW164, -165, -409

Data are given in km/Ma

Supplementary information

Supplementary information accompanies this paper at https://doi.org/10.1186/s00015-020-00356-4.

Additional file 1: Appendix S1. Details on the RSCM analysis and data processing procedures used.

Acknowledgements
We thank François Negro for contributing unpublished RSCM data. We thank Meinert Rahn and an anonymous reviewer for the careful and detailed reviews. We also acknowledge the help of the editor Edwin Gnos.

Authors' contributions
AB, ME, MH designed the study. SE, CG and CS measured and/or helped with the fission track measurements and sampling. RG measured RCMS data and add field data. AB, ME, MH, CG wrote the article. All authors read and approved the final manuscript.

Funding
We gratefully acknowledge funding by the Swiss National Science Foundation (Projects 1132196, 109637 and 149385).

Availability of data and materials
All used data are available in the manuscript.

Ethics approval and consent to participate
Not applicable.

Consent for publication
Not applicable.

Competing interests
The authors declare no competing interests.

Author details
[1] Institute of Geological Sciences, University of Bern, Baltzerstrasse 1 + 3, 3012 Bern, Switzerland. [2] Department of Geosciences, University of Tuebingen, Wilhelmstrasse 56, 72074 Tübingen, Germany. [3] Department of Geowissenschaften, University of Bremen, Klagenfurter Str. 2, 28359 Bremen, Germany.

Received: 11 September 2019 Accepted: 7 March 2020
Published online: 06 April 2020

References

Allaz, J., Engi, M., Berger, A., & Villa, I. M. (2011). The effects of retrograde reactions and of diffusion on $^{40}Ar/^{39}Ar$ ages of micas. *Journal of Petrology, 52,* 691–716.
Berger, A., Gnos, E., Janots, E., Whitehouse, M., Soom, M., Frei, R., et al. (2013). Dating brittle tectonic movements with cleft monazite: Fluid–rock interaction and formation of REE minerals. *Tectonics, 32,* 1–14.
Berger, A., Mercolli, I., Herwegh, M., & Gnos, E. (2017). *Geological map of the Aar Massif, Tavetsch and Gotthard nappes (1:100000). Explanatory notes*. Wabern: Landesgeologie Schweiz.
Berger, A., Schmid, S. M., Engi, M., Bousquet, R., & Wiederkehr, M. (2011). Mechanisms of mass and heat transport during Barrovian metamorphism: A discussion based on field evidence from the Central Alps (Switzerland/Northern Italy). *Tectonics, 30,* TC1007.
Beyssac, O., Goffé, B., Chopin, C., & Rouzaud, J. N. (2002a). Raman spectra of carbonaceous material in metasediments: A new geothermometer. *Journal of Metamorphic Geology, 20,* 859–871.
Beyssac, O., Rouzaud, J. N., Goffé, B., Brunet, F., & Chopin, C. (2002b). Graphitization in a high-pressure, low-temperature metamorphic gradient: A Raman micro-spectroscopy and HRTEM study. *Contributions to Mineralogy Petrology, 143,* 19–31.
Boston, K., Rubatto, D., Hermann, J., Engi, M., & Amelin, Y. (2017). Geochronology of accessory allanite and monazite in the Barrovian metamorphic sequence of the Central Alps, Switzerland. *Lithos, 286–287,* 502–518.
Bousquet, R., et al. (2012). Metamorphic framework of the Alps, Map of CCGM/CGMW.
Bousquet, R., Oberhänsli, R., Goffé, B., Wiederkehr, M., Koller, F., Schmid, S. M., et al. (2008). Metamorphism of metasediments in the scale of an orogen: A key to the Tertiary geodynamic evolution of the Alps. Tectonic aspects of the alpine–carpathian-dinaride system. *Geological Society London, Special Publication, 298,* 393–411.
Brandon, M. T., Roden-Tice, M. K., & Garver, J. I. (1998). Late Cenozoic exhumation of the Cascadia accretionary wedge in the Olympic Mountains, northwest Washington State. *Geological Society of America Bulletin, 110,* 985–1009.
Braun, J., van der Beek, P., & Batt, G. (2006). *Quantitative thermochronology* (p. 258). Cambridge: Cambridge University Press.
Burkhard, M. (1988). L'Helvetique de la bordure occidentale du massif de l'Aar (e´volution tectonique et me´tamorphique). *Eclogae geologae Helvetiae, 81,* 63–114.
Campani, M., Mancktelow, N. S., & Courrioux, G. (2014). The 3D interplay between folding and faulting in a syn-orogenic extensional system: the Simplon Fault Zone in the Central Alps (Switzerland and Italy). *Swiss Journal of Geoscience, 107,* 251–271.
Campani, M., Mancktelow, N., Seward, D., Rolland, Y., Muller, W., & Guerra, I. (2010). Geochronological evidence for continuous exhumation through the ductile/brittle transition along a crustal-scale low-angle normal fault: Simplon Fault Zone, central Alps. *Tectonics, 29,* TC3002. https://doi.org/10.1029/2009tc002582.
Champagnac, J. D., Sue, C., Delacou, B., & Burkhard, M. (2003). Brittle orogen-parallel extension in the internal zones of the Swiss Alps (south Valais). *Eclogae geologae Helvetiae, 96,* 325–338.
Chatterjee, N. D. (1961). The Alpine metamorphism in the Simplon area, Switzerland and Italy. *Geologische Rundschau, 51,* 1–72.
Diehl, T., Clinton, J., Deichmann, N., Cauzzi, C., Kästli, P., Kraft, T., et al. (2018). Earthquakes in Switzerland and surrounding regions during 2015 and 2016. *Swiss Journal of Geosciences, 111,* 221–244.
Dolivo, E. (1982). Nouvelles observations structurales au SW du massif de l'Aar entre Visp et Gampel. *Beitr. Geolog. Karte Schweiz (N.F.), 157,* 1–82.
Dunkl, I. (2002). Trackkey: A windows program for calculation and graphical presentation of fission track data. *Computer Geoscience, 28,* 3–12. https://doi.org/10.1016/S0098-3004(01)00024-3.
Engi, M. (2011). Structure et évolution métamorphique des Alpes Centrales. *Géochronique, 117,* 22–26.
Engi, M., Lanari, P., & Kohn, M. (2017). Significant ages—An introduction to petrochronology. *Reviews in Mineralogy and Geochemistry, 83,* 1–12.
Erne, S. (2014). Temperaturabschätzung der Metasedimente zwischen Gotthard- und Aar-Massiv in der Urseren-Garvera Zone, mittels Ramanspektroskopie. Bachelor thesis, unpublished. Universität Bern.
Frank, E., & Stettler, A. (1979). K–Ar and ^{39}Ar–^{40}Ar systematics of white K-mica from an Alpine metamorphic profile in the Swiss Alps. *Schweizerische Mineralogische und Petrographische Mitteilungen, 59,* 375–394.

Frey, M., Desmons, J., & Neubauer, F. (1999). The new metamorphic map of the Alps: Introduction. *Schweizerische Mineralogische und Petrographische Mitteilungen, 79,* 1–4.
Frey, M., Teichmueller, M., Teichmueller, R., Mullis, J., Kuenzi, B., Breitschmid, A., et al. (1980). Very-low grade metamorphism in external parts of the Central Alps: Illite crystallinity, coal rank and fluid inclusion data. *Eclogae Geologicae Helvetiae, 73,* 173–203.
Giese, J., Seward, D., Stuart, F. M., Wüthrich, E., Gnos, E., & Kurz, D. (2010). Electrodynamic disaggregation: Does it affect apatite fission-track and (U–Th)/he analyses? *Geostandards and Geoanalytical Research, 34,* 39–48.
Girault, J. B., Bellahsen, N., Boutoux, A., Rosenberg, C., Nanni, U., Verlaguet, A., et al. (2020). 3D thermal structure of the Helvetic nappes of the European Alps: Implications for collisional processes. *Tectonics, 39,* e2018TC005334. https://doi.org/10.1029/2018TC005334.
Hafner, S. (2016). *The thermal peak in metamorphic black shales: Gradients in the Valaisan units and the contrast to tectonic neighbors*. Master Thesis University of Bern, 117 pp.
Herwegh, M., Berger, A., Wehrens, P., Baumberger, R., & Kissling, E. (2017). Large-scale crustal-block-extrusion during late Alpine collision. *Scientific Reports, 7,* 413–418.
Herwegh, M., Kissling, E., Baumberger, R., Berger, A., Wangenheim, C., Wehrens, P., et al. (2020). Late stages of continent-continent collision: Timing, kinematic evolution and exhumation of the Northern rim of the Alps. *Earth Science Review, 200,* 102959.
Herwegh, M., & Pfiffner, O. A. (2005). Tectono-metamorphic evolution of a nappe stack: A case study of the Swiss Alps. *Tectonophysics, 404,* 55–76.
Hurford, A. J., & Green, I. R. (1983). The zeta age calibration of fission track dating. *Isotope Geosciences, 1,* 285–317.
Janots, E., Engi, M., Rubatto, D., Berger, A., Gregory, C., & Rahn, M. (2009). Metamorphic rates in collisional orogeny from in situ allanite and monazite dating. *Geology, 37,* 11–14.
Jaquet, Y., Duretz, T., Grujic, D., Masson, H., & Schmalholz, S. M. (2017). Formation of orogenic wedges and crustal shear zones by thermal softening, associated topographic evolution and application to natural orogens. *Tectonophysics, 746,* 512–529.
Kirschner, D., Masson, H., & Cosca, M. (2003). An $^{40}Ar/^{39}Ar$, Rb/Sr, and stable isotope study of micas in low-grade fold-and-thrust belt: An example from the Swiss Helvetic Alps. *Contributions to Mineralogy and Petrology, 145,* 460–480.
Kohn, M. (2014). Himalayan metamorphism and its tectonic implications. *Annual Review Earth Planetary Science, 42,* 381–419.
Krayenbuhl, T., & Steck, A. (2009). Structure and kinematics of the Jungfrau syncline, Faflertal (Valais, Alps), and its regional significance. *Swiss Journal of Geosciences, 102,* 441–455.
Mair, D., Lechmann, A., Herwegh, M., Nibourel, L., & Schlunegger, F. (2018). Linking Alpine deformation in the Aar Massif basement and its cover units—The case of the Jungfrau-Eiger mountains (Central Alps, Switzerland). *Solid Earth, 9,* 1099–1122.
Malusa, M. G., & Fitzgerald, P. G. (2019). *Fission-track thermochronology and its application to geology*., Springer textbooks in earth sciences, geography and environment Cham: Springer.
Mancktelow, N. S. (1990). The Simplon fault zone. *Beitr. Geol. Karte Schweiz, 163,* 1–74.
Mancktelow, N. S. (1992). Neogene lateral extension during convergence in the central Alps: Evidence from interrelated faulting and backfolding around the Simplon pass (Switzerland). *Tectonophysics, 215,* 295–317.
Marsellos, A. E., & Garver, J. I. (2010). Radiation damage and uranium concentration in zircon as assessed by Raman spectroscopy and neutron irradiation. *American Mineralogist, 95,* 1192–1201.
Michalski, I., & Soom, M. (1990). The Alpine thermo-tectonic evolution of the Aar and Gotthard massifs, Central Switzerland: fission track ages on zircon and apatite and K–Ar mica ages. *Schweizerische Mineralogische und Petrographische Mitteilungen, 70,* 373–387.
Milnes, A. G. (1973). Structural re-interpretation of the classic Simplon tunnel section of the Central Alps. *Geological Society America, Bullettin, 84,* 269–274.
Milnes, A. G. (1974). Structure of the Pennine Zone: A new working hypothesis. *Geological Society America, Bullettin, 85,* 1727–1732.
Milnes, A. G. (1975). On steep isograde surfaces in the Simplon area: A discussion. *Contributions to Mineralogy and Petrology, 53,* 65–70.
Negro, F., Bousquet, R., Vils, F., Pellet, C.-M., & Hänggi-Schaub, J. (2013). Thermal structure and metamorphic evolution of the Piemont-Ligurian metasediments in the northern Western Alps. *Swiss Journal of Geosciences, 106,* 63–78.
Nibourel, L. (2019). The structural and thermo-kinematic evolution of the eastern Aar Massif, Switzerland. Ph.D. University of Bern, 137 pp.
Nibourel, L., Berger, A., Egli, D., Luensdorf, N. K., & Herwegh, M. (2018). Large vertical displacements in the Aar Massif recorded by Raman thermometry. *Geology, 46,* 879–882.
Niggli, E., & Niggli, C. (1965). Karten der Verbreitung einiger Mineralien der alpidischen Metamorphose in den Schweizer Alpen (Stilpnomelan, Alkali-Amphibol, Chloritoid, Staurolith, Disthen, Sillimanit). *Eclogae Geologicae Helvetiae, 58,* 335–368.
Pfiffner, O. A. (2015). *Geologie der Alpen* (p. 360). Bern: UTB/Haupt Verlag.
Rahn, M. K. (2001). *The metamorphic and exhumation history of the Helvetic Alps, Switzerland, as revealed by apatite and zircon fission tracks*. Habilitation thesis, Albert-Ludwigs-Universität Freiburg, 140 pp.
Rahn, M. K., Brandon, M. T., Batt, G. E., & Garver, J. I. (2004). A zero damage model for fission-track annealing in zircon. *American Mineralogist, 89,* 473–484.
Rahn, M. K., Wang, H., & Dunkl, I. (2019). A natural long-term annealing experiment for the zircon fission track system in the Songpan-Garzê flysch, China. *Terra Nova, 31,* 295–305.
Reinecker, J., Danisik, M., Schmid, C., Glotzbach, C., Rahn, M., Frisch, W., et al. (2008). Tectonic control on the late stage exhumation of the Aar Massif (Switzerland): Constraints from apatite fission track and (U-Th)/He data. *Tectonics, 27,* TC6009.
Ricchi, E., Bergemann, C. A., Gnos, E., Berger, A., Rubatto, D., & Whitehouse, M. J. (2019). Constraining deformation phases in the Aar Massif and the Gotthard Nappe (Switzerland) using Th–Pb crystallization ages of fissure monazite-(Ce). *Lithos, 342–343,* 223–238.
Rolland, Y., Cox, S. F., & Corsini, M. (2009). Constraining deformation stages in brittle ductile shear zones from combined field mapping and 40Ar/39Ar dating: The structural evolution of the Grimsel Pass area (Aar Massif, Swiss Alps). *Journal of Structural Geology, 31,* 1377–1394.
Roselle, G. T., Thüring, M., & Engi, M. (2002). MELONPIT: A finite element code for simulating tectonic mass movement and heat flow within subduction zones. *American Journal of Science, 302,* 381–409.
Sartori, M., Marthaler, M., Gouffon, Y., Meisser, N. (2017). Blatt 1288 Raron.- Geol. Atlas der Schweiz: Erläuterungen 153, 140 pp.
Schmalholz, S. M., & Duretz, T. (2015). Shear zone and nappe formation by thermal softening, related stress and temperature evolution, and application to the Alps. *Journal of Metamorphic Geology, 33,* 887–908.
Schmidt, C. & Preiswerk, H. (1905). Geologische Karte der Simplongruppe. *Beiträge zur Geologischen Karte der Schweiz, [N.F.] 26*, Spezialkarte No. 48.
Shi, Y., & Wang, C. Y. (1987). Two-dimensional modeling of the P-T-t paths of regional metamorphism in simple overthrust terrains. *Geology, 15,* 1048–1051.
Soom, M. A. (1990). *Abkühlungs- und Hebungsgeschichte der Externmassive und der penninischen Decken beidseits der Simplon-Rhone-Linie seit dem Oligozän: Spaltspurdatierung and Apatit/Zirkon und K–Ar-Datierungen an Biotit/Muskovit (westliche Zentralalpen)*. Bern, Switzerland, University of Bern, Ph.D. Thesis, 64 p.
Steck, A. (1984). Tertiary deformation structures in the central Alps. *Eclogae Geologicae Helvetiae, 77,* 55–100.
Steck, A. (2008). Tectonics of the Simplon massif and Lepontine gneiss dome: Deformation structures due to collision between the underthrusting European plate and the Adriatic indenter. *Swiss Journal of Geosciences, 101,* 515–546.
Steck, A., Epard, J.L., Escher, A., Gouffon, Y., & Masson, H. (2001). Notice explicative de la Carte tectonique des Alpes de Suisse occidentale et des regions avoisinantes 1: 100'000, Carte géologique spéciale N. 123. 73 pp.
Streckeisen, A., Wenk, E., & Frey, M. (1974). On steep isogradic surfaces in the Simplon area. *Contributions to Mineralogy and Petrology, 47,* 81–95.
Tagami, T., & Matsu´ura, S. (2019). Thermal annealing characteristics of fission tracks in natural zircons of different ages. *Terra Nova, 31,* 257–262.
Todd, C. S., & Engi, M. (1997). Metamorphic field gradients in the Central Alps. *Journal of Metamorphic Geology, 15,* 513–530.
Vance, D., & O'Nions, R. K. (1992). Prograde and retrograde thermal histories from the Central Swiss Alps. *Earth and Planetary Science Letters, 114,* 113–129.

Villa, I. M., Bucher, S., Bousquet, R., Kleinhanns, I., & Schmid, S. M. (2014). Dating polygenetic metamorphic assemblages along a transect across the Western Alps. *Journal of Petrology, 55,* 803–830.
Wagner, G. A., Reimer, G., & Jäger, E. (1977). Cooling ages derived by apatite fission track, mica Rb-Sr and K-Ar dating: The uplift and cooling history of the Central Alps. *Memorie degli Istituti di Geologia e Minalogia dell' Universita´ di Padova, 30,* 1–27.
Wagner, A. G., & van de Haute, P. (1992). *Fission-track dating*. Stuttgart: Ferdinand Enke Verlag.
Wang, A., Dhamelincourt, P., Dubessy, J., Guerard, D., Landais, P., & Lelaurain, M. (1989). Characterization of graphite alteration in an uranium deposit by micro-Raman spectroscopy, X-RAY diffraction, Transmission Electron Microscopy and Scanning Electron Microscopy. *Carbon, 27,* 209–218.
Wehrens, P., Baumberger, R., Berger, A., & Herwegh, M. (2017). How is strain localized in a mid-crustal basement section? Spatial distribution of deformation in the Aar massif (Switzerland). *Journal of Structural Geology, 94,* 47–67.
Wicki, A. (2014). *Raman-Messungen an organischem Material aus dem Helvetikum*. Bachelor Thesis, Universität Bern.
Wiederkehr, M., Bousquet, R., Schmid, S. M., & Berger, A. (2008). From subduction to collision: Thermal overprint of HP/LT meta-sediments in the north-eastern Lepontine Dome (Swiss Alps) and consequences regarding the tectono-metamorphic evolution of the Alpine orogenic wedge. *Swiss Journal of Geosciences, 100,* 1–29.
Wiederkehr, M., Bousquet, R., Ziemann, M. A., Berger, A., & Schmid, S. M. (2011). 3-D assessment of peak-metamorphic conditions by Raman spectroscopy of carbonaceous material: An example from the margin of the Lepontine dome (Swiss Central Alps). *International Journal of Earth Science, 100,* 1029–1063.
Wiederkehr, M., Sudo, M., Bousquet, R., Berger, A., & Schmid, S. M. (2009). Alpine orogenic evolution from subduction to collisional thermal overprint: the Ar40/Ar39 age constraints from the Valaisan Ocean, Central Alps. *Tectonics, 28,* TC6009.
Williams, D. J. A., Hofmann, B. A., & Glasspool, I. G. (2008). Coalification in carboniferous sediments from the Lötschberg base tunnel. *Swiss Journal of Geosciences, 101,* 651–658.
Ziegler, H.-J., & Isler, A. (2013). Lötschberg Basistunnel - zusammenfassender geologischer Schlussbereicht. *Berichte der Landesgeologie, 4,* 1–92.

Publisher's Note